Japanese Journal of Applied Physics

REGULAR PAPER

The ferroelectric orthorhombic phase formation of $Hf_{0.5}Zr_{0.5}O_2$ thin films on (−201) β-Ga_2O_3 substrate by atomic layer deposition

To cite this article: K. Naito *et al* 2023 *Jpn. J. Appl. Phys.* **62** SM1018

Japanese Journal of Applied Physics **62**, SM1018 (2023) **REGULAR PAPER**
https://doi.org/**10.35848/1347-4065/ace917**

The ferroelectric orthorhombic phase formation of $Hf_{0.5}Zr_{0.5}O_2$ thin films on (−201) β-Ga_2O_3 substrate by atomic layer deposition

K. Naito[1], K. Yamaguchi[2], T. Yoshimura[1], and N. Fujimura[1*]

[1]*Department of Physics and Electronics, Graduate School of Engineering, Osaka Metropolitan University, Sakai 599-8531, Japan*
[2]*Department of Physics and Electronics, Graduate School of Engineering, Osaka Prefecture University, Sakai 599-8531, Japan*

*E-mail: fujim@omu.ac.jp

Received June 6, 2023; revised July 18, 2023; accepted July 20, 2023; published online August 9, 2023

The orthorhombic (O) phase formation process of $Hf_{0.5}Zr_{0.5}O_2$ (HZO) thin films on Ga_2O_3 substrate is demonstrated. As deposited HZO thin film has the O and tetragonal (T) phases together with an amorphous phase and post-metallization annealing suppresses the crystallization into the T phase and promotes the O phase compared to annealing without a top electrode. Positive-up-negative-down measurement reveals that remanent polarization for the downwards (accumulation side) only originates from the ferroelectricity in HZO films on Ga_2O_3 substrate. Using normal capacitance–voltage (*C–V*) measurements, a clear capacitance change from accumulation to depletion was observed. However, the *C–V* results also show clockwise hysteresis by charge injection from the semiconductor. High-speed *C–V* measurements at a voltage sweep frequency above 3 Hz show counterclockwise hysteresis, and hysteresis width saturates as the applied voltage increases. Based on these results, HZO thin films with O phase on Ga_2O_3 substrates have ferroelectricity.

1. Introduction

Internet of Things (IoT) technologies and artificial intelligence (AI) play important roles in different aspects of our lives. In the current IoT society, the information produced is analyzed by cloud computing, but as the number of IoT applications increases, the enormous scale of that information heavily burdens the cloud servers and causes much greater power consumption. Consequently, edge computing has attracted attention as a way to reduce these burdens.[1–3] Edge devices need to have low power consumption, so nonvolatile devices are required to suppress the consumption of power-off data storage. In addition, edge devices are required to process huge volumes of data rapidly with AI, and reservoir computing plays an important role in this process.[4,5] The ferroelectric FET (FeFET) is one candidate device that meets such requirements.[6,7]

Although many researchers have studied FeFETs using ferroelectric materials such as Pb(Zr, Ti)O_3 (PZT), $SrBi_2Ta_2O_9$ (SBT), and $YMnO_3$ (YMO),[8–10] none have yet been able to put these devices into practical use due to three major problems: (1) the formation of an interfacial layer with low dielectric constant at the ferroelectric/semiconductor interface;[11] (2) the enhancement of the depolarization field by the interfacial layer;[12,13] and (3) limitations of device size caused by the thickness effect of ferroelectric films.[14] In relation to this third issue, however, the discovery of Hf-based films that exhibit ferroelectricity even when the thickness is below 10 nm has prompted dramatic improvement.[15,16] Although studies on HfO_2-based FeFETs have been enthusiastically pursued,[17–22] the first and second issues still exist.[18] To overcome them, the use of oxide semiconductors, such as ZnO, has been reported to avoid the formation of the interfacial layer with a low dielectric constant.[23] We are interested in the use of Ga_2O_3 as an oxide semiconductor for the power device application of an HfO_2-based FeFET.[24–26]

A metal-ferroelectric-insulator-semiconductor structure with HfO_2-based ferroelectric/low-*k* dielectric layer (Al_2O_3)/Ga_2O_3 has been previously studied,[27–29] but the interface of a HfO_2-based ferroelectric/Ga_2O_3 has not.[30] In reports of the structure of high-*k* HfO_2/Ga_2O_3 metal-insulator-semiconductor capacitors, the conduction band offset is around 1.3 eV, which indicates that HfO_2-based films are applicable as the gate dielectric layer of a Ga_2O_3 MOSFET.[31–33] In contrast, the VB offset at below 0.5 eV is too low to inhibit the leakage current when the semiconductor is inverted. In the case of Ga_2O_3 semiconductors, however, the acceptor level (1.3 eV) is too low to activate the acceptor,[34,35] so it is extremely important to study how ferroelectric polarization switching progresses and how the band diagrams of the semiconductor change.

The ferroelectricity of HfO_2 presents in the metastable orthorhombic phase (O);[15] however, no reports exist on the formation of the ferroelectric O phase directly on a Ga_2O_3 substrate. The behavior of HfO_2-based ferroelectric polarization switching on wide-bandgap semiconductors without the formation of inversion layers is also of great interest. In this paper, we report the phase formation process of $Hf_{0.5}Zr_{0.5}O_2$ (HZO) thin films on (−201) β-Ga_2O_3 substrate by atomic layer deposition (ALD).

2. Experimental methods

An unintentionally doped (−201) β-Ga_2O_3 substrate was cleaned using ultrasonic organic solution (acetone/methanol/deionized water) and a sulfuric peroxide mix acid solution (96% H_2SO_4:30%H_2O_2:H_2O = 4:1:1). It was then annealed at 950 °C for 30 min under nitrogen atmosphere to obtain a step-and-terrace structure with a step height of 4.8 Å, corresponding to the lattice spacing of bulk Ga_2O_3. Subsequently, 15 nm-HZO thin films were fabricated on the (−201) β-Ga_2O_3 substrate using thermal ALD (GEMStar XT-R, Arradiance; Littleton, MA). Tetrakis-ethylmethylamino hafnium (TEMAHf), tetrakis-ethylmethylamino zirconium (TEMAZr), and H_2O were used as precursors of Hf, Zr, and oxidants, respectively.[36,37] In the ALD method, the deposition conditions, such as the pulse and purge times of the precursors and the substrate temperature, are determined by whether the film growth is saturated or not, and this is called the ALD window.[38] Therefore, we fabricated HfO_2 and ZrO_2 thin films on a (001) Si substrate by first changing various conditions to find the ALD window. According to the fundamental optimization of the deposition conditions, the ALD conditions shown in Table I were used in this work.

$Hf_{0.5}Zr_{0.5}O_2$ thin films were fabricated by alternately stacking HfO_2 and ZrO_2 layers 150 times at 280 °C. After HZO film fabrication, rapid thermal annealing (RTA) in N_2 ambient conditions was performed for 30 s at 700 °C in a process known as post-deposition annealing (PDA). For some samples, a platinum top electrode was fabricated by RF magnetron sputtering, and then RTA in N_2 ambient conditions was performed for 30 s at temperatures ranging from 500 °C to 700 °C. This process is known as post-metallization annealing (PMA), and indium was then soldered as the bottom electrode to form an ohmic contact. The crystallization phase of the HZO thin films was characterized by grazing incidence X-ray diffraction (GIXRD; SmartLab, Rigaku; Tokyo, Japan). Positive-up-negative-down (PUND) measurements were carried out using a function generator (WF 1948, NF Co.; Kanagawa, Japan) to accurately evaluate remanent polarization without the effect of leakage current.[39–41] Capacitance–voltage (*C–V*) characteristics for the Pt/HZO/β-Ga_2O_3/In MFS structure were measured at 10 kHz using an LCR meter (HP4140B, Hewlett Packard; Palo Alto, Ca). High-speed *C–V* measurements with a voltage sweeping rate of 0.05–10 Hz were performed using a *C–V* analyzer (KEITHLEY 590; Tokyo, Japan).

3. Results and discussion

Figure 1 illustrates the effect of annealing temperature, showing the GIXRD patterns of as deposition (as-depo.)-HZO (blue line), PDA-HZO (green line), and PMA-HZO (red lines) thin films fabricated at 280 °C on (−201) β-Ga_2O_3 substrates. In the case of as-depo.-HZO (blue line), the strongest diffraction peak was at 30.7°, and the shoulder was recognized at around 30.5°. These diffractions correspond to the non-equilibrium, O, and T phases. Because the lattice spacing of the T phase is shorter than that of the O phase, the strongest and shoulder peaks correspond to the T (2θ = 30.7°) and O (2θ = 30.5°) phases, respectively. Therefore, the as-depo.-HZO crystallizes to the O+T phases, but it should include an amorphous phase from previous studies.[42] The small and broad diffraction peaks between 31.5° and 32.0° seem to be mixed diffraction from the 111 M phase and 002 T phase.[43] After PDA treatment at 700 °C, the thin film crystallizes into the M (2θ = 28.5° and 31.5°) and T (2θ = 33.0°) phases, as shown by the green line in Fig. 1.

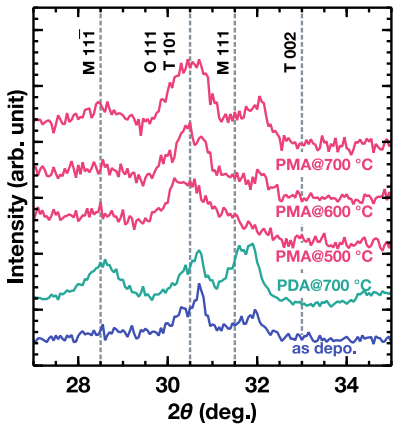

Fig. 1. GIXRD patterns of HZO thin films annealed at different temperatures fabricated on a (−201) β-Ga_2O_3 substrate.

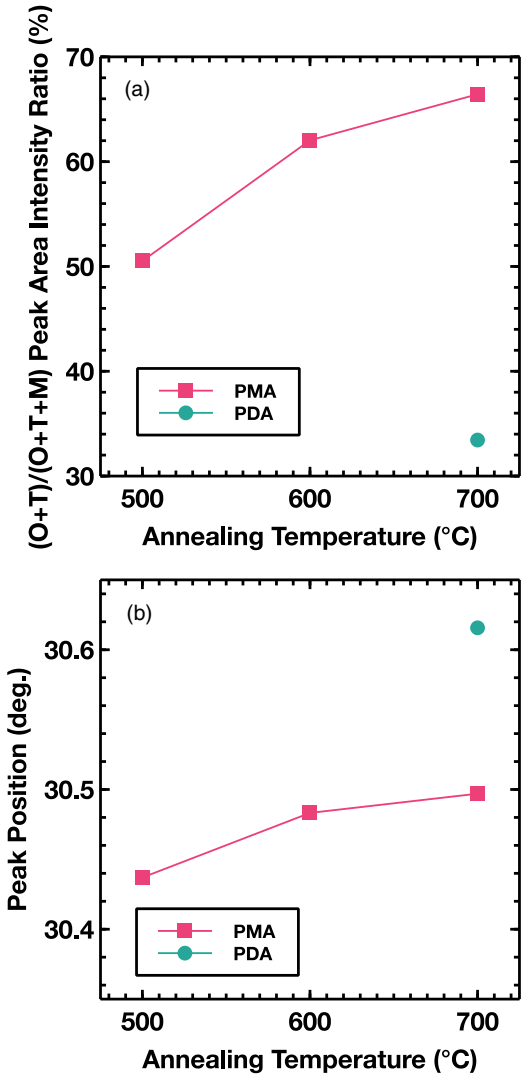

Fig. 2. (a) Percentage of O+T phases against total peak area intensity of HZO thin films after PDA and PMA treatment, as calculated from GIXRD patterns. (b) Changes in diffraction peak position (2θ = 30.5°) of the O+T phases.

Therefore, PDA enhances transformation to a stable phase, as in many existing reports.[44,45]

After PMA treatment at temperatures ranging from 500 °C to 700 °C, however, crystallization into the O phase was observed, as shown by the red line in Fig. 1. The amorphous phase in the as-deposited thin film crystallized mainly into the O phase and partially into the T phase because the diffraction peak at around 30.5° became larger after PMA treatment. Figure 2(a) shows the percentage of the O+T phases against total peak area intensity. The percentage of the O+T phases increased from 50% to 70% with the increase in temperature from 500 °C to 700 °C. The broad diffraction peak at 30.5° in PMA at 500 °C shifts to a higher angle with increasing temperature, as shown in Fig. 2(b). Since the lattice spacing of the T phase is smaller than that of the O phase, this peak shift indicates that the phasing of HZO thin films changes from the O phase to the T phase with increasing PMA temperature. Focusing on an annealing temperature of 700 °C, the volume fraction of the O phase for the PMA sample is larger than that of the O phase for the PDA sample. In contrast, the volume fraction of the T phase for the PMA sample is smaller than that of the T phase for the

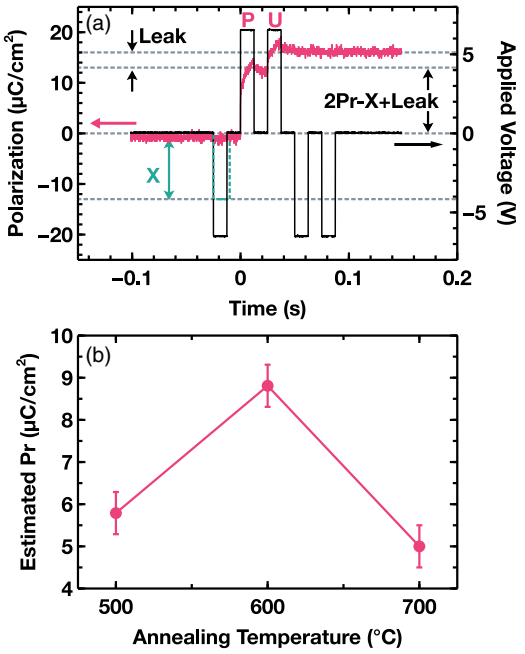

Fig. 3. (a) PUND measurement of Pt/HZO/Ga_2O_3/In MFSM structure. (b) Estimated polarization evaluation of PMA-HZO thin films with increasing annealing temperatures.

PDA sample. As a result, the peak of the O+T phases at 30.5°–30.7° shifts to a higher angle. The results suggest that PMA treatment is more effective than PDA in terms of suppressing the development of the T phase. From the GIXRD measurements, we can conclude that the annealing temperature at a maximum volume fraction of the O phase exists between 500 °C and 700 °C and that PMA treatment is an effective way to form a metastable phase.

Table I. The ALD conditions used in this work.

Precursors	TEMAHf	TEMAZr	H_2O
Pulse time	1250 ms	1050 ms	60 ms
Purge time	25 s	25 s	25 s
Precursor temperature	90 °C	90 °C	R.T.
Carrier gas	N_2 (40 sccm)	N_2 (40 sccm)	N_2 (40 sccm)

To ascertain whether or not the O phase is ferroelectric with remanent polarization, PUND measurement was carried out for the PMA-HZO fabricated on (−201) β-Ga_2O_3 substrates. In PUND evaluation, four kinds of bias (positive, up, negative, and down) are applied in succession to the sample using the Sawyer-tower circuit. By applying two voltage pulses with the same polarity in sequence, it is possible to eliminate the leakage current component from the apparent remanent polarization.[39–41] Based on fundamental experiments on the effect of pulse width and voltage, two clear remanent polarizations can be recognized by subtracting the two leakage components from the polarization differences

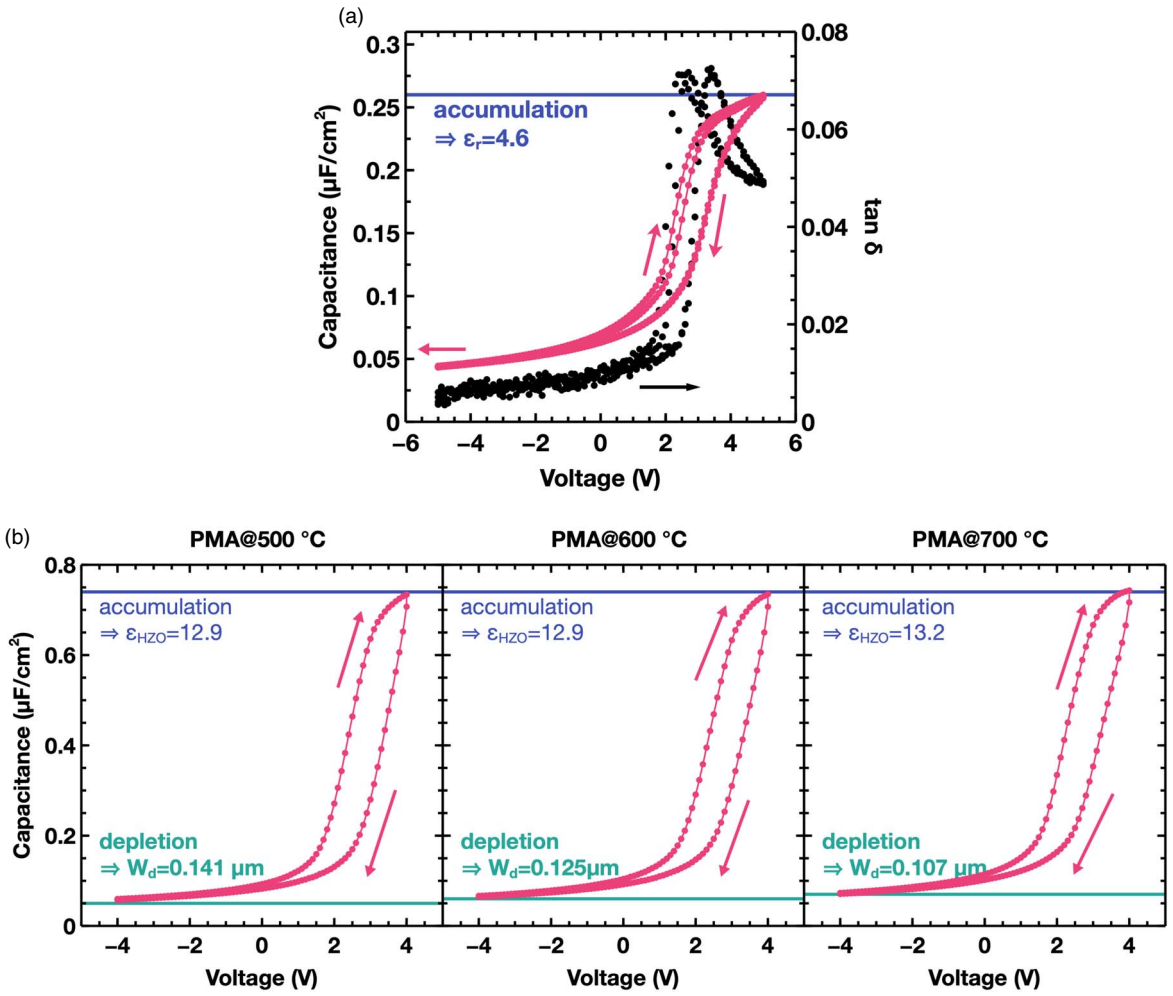

Fig. 4. *C–V* characteristics of (a) as-depo.-HZO and (b) PMA-HZO films annealed at 500 °C, 600 °C, and 700 °C.

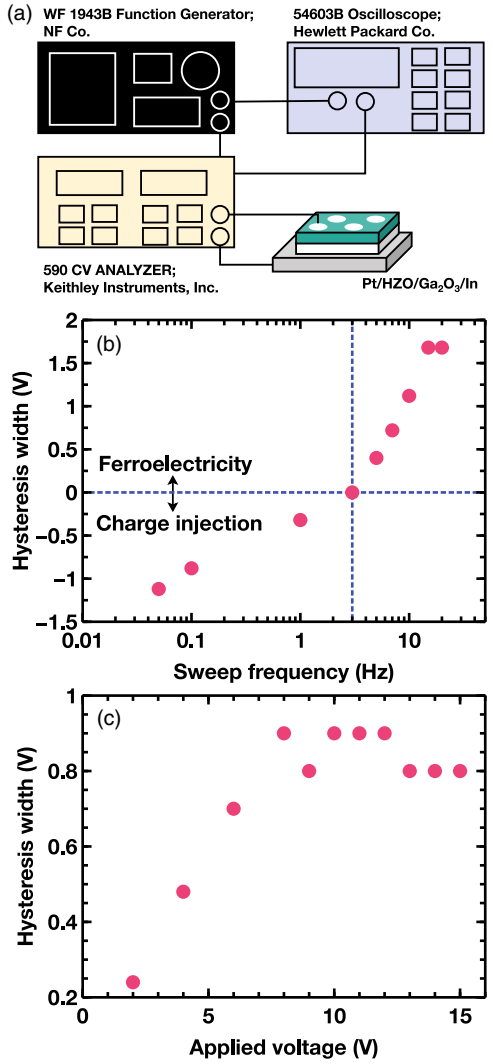

Fig. 5. (a) A schematic image of a high-speed capacitance measurement system, and *C*–*V* hysteresis width when (b) the sweep frequency is changed and (b) when the applied voltage at a bias sweep frequency of 7 Hz is changed.

obtained from the positive and negative biases when pulse width and voltage are 12.5 ms and 6 V, respectively.

Figure 3(a) illustrates the PUND results of the PMA-HZO film annealed at 600 °C. Normally, polarization switches when a negative bias is applied, but in this structure, switching does not occur. We assume that this is because minority carriers in Ga_2O_3 are not excited, and the band offset is very small, as mentioned in the Introduction section. Subsequently, applying a positive bias produces a downward polarization component (P), as shown in Fig. 3(a), but the polarization hardly decreases before the next bias is applied. By applying the up bias, the amount of downward polarization (U) further increases [Fig. 3(a)], although the direction of polarization remains unchanged after the application of the negative and down voltages. In order to estimate the ferroelectric-induced polarization, the difference between the P and U polarization is used as the leakage component (Leak) and subtracting that from the P polarization calculates the amount of estimated polarization. Figure 3(b) shows the change in estimated polarization with increasing annealing temperature. These results indicate that the PMA-HZO annealed at 600 °C has the maximum volume fraction of the O phase and that polarization is approximately the largest. In this measurement, the effect of the depletion layer was large and negative polarization was not recognized; therefore, *C*–*V* evaluations were carried out to understand the ferroelectric behavior of the HZO films on Ga_2O_3 substrate.

Figure 4(a) shows the *C*–*V* characteristics of the as-depo.-HZO film. In the black line from the right-hand axis, the loss tangent is below 0.1, suggesting that this film has relatively good insulation. The left-hand axis corresponds to the normalized capacitance, denoted by the red line. By calculating accumulation capacitance, the relative permittivity of the 15 nm-HZO films was found to be 4.6, which is quite low compared to the 10–20 of the HZO thin films, suggesting that the main crystallization phase of the film is amorphous, as mentioned in the GIXRD measurement section above. As shown in Fig. 4(b), PMA treatment increased relative permittivity to 13, and this did not change depending on the annealing temperature. This indicates that the crystallization of the amorphous phase is almost complete, and that relative permittivity is independent of the change from the O to T phases. The depletion layer width, calculated from the depletion capacitance, slightly decreased from 0.14 to 0.11 μm with increasing PMA temperature.

However, these *C*–*V* characteristics show a clockwise hysteresis curve originating mainly from charge injection from the semiconductor. It was assumed that the hysteresis included the effect of ferroelectric polarization switching and that the charge injection would be strongly affected by the bias voltage sweep rate, so high-speed *C*–*V* measurements at sweep frequencies from 0.05 to 10 Hz were performed using a *C*–*V* analyzer. Figure 5(a) shows a schematic image of a high-speed capacitance measurement system. The *C*–*V* characteristics at a sweep frequency of 0.05 Hz display clockwise hysteresis, as shown in Fig. 4, which was defined as negative. Figure 5(b) illustrates the change in hysteresis width with increasing sweep frequency. The hysteresis changes from clockwise to counterclockwise as sweep frequency increases,[46] and its width changes from negative to positive at 3 Hz, suggesting that counterclockwise hysteresis originating from ferroelectric domain switching is dominant at frequencies above 3 Hz. Figure 5(c) shows the effect of applied voltage on hysteresis width at a sweep frequency of 7 Hz, where the main contributor to the hysteresis is ferroelectricity rather than charge injection. Hysteresis width increased with increasing applied voltage and saturated at 0.8–0.9 V. Based on these results, hysteresis measured above 3 Hz is mainly derived from ferroelectricity.

4. Conclusions

The GIXRD results indicate that the as-depo.-HZO thin film has the O+T and amorphous phases and that the amorphous phase crystallizes into the M or O+T phases by PDA or PMA treatment, respectively. In addition, PMA treatment suppresses crystallization into the T phase and promotes crystallization into the O phase, as compared to PDA. Therefore, PMA treatment can be said to enhance the formation of a metastable O phase. The PUND results show that the HZO films with an O phase have remanent polarization when the positive and up biases are applied. The estimated polarization of PMA-HZO at 600 °C had the largest value, suggesting the maximum volume fraction of the O phase in this film. When the negative and down biases are applied, however, polarization switching is not recognized, probably because minority

carriers in Ga_2O_3 are not excited and the band offset is very small. Furthermore, analysis of the high-speed *C*–*V* characteristics confirmed counterclockwise hysteresis at bias voltage sweep frequencies above 3 Hz. The hysteresis width saturated when the applied voltage was 7 V. Based on these results, we conclude that the HZO films with the O phase on Ga_2O_3 substrate have ferroelectricity.

Acknowledgments

This work was supported by MIC research and development (JPMI00316).

1) G. Yashodha, P. R. Pameel Rani, A. Lavanya, and V. Sathyavathy, IOP Conf. Ser.: Mater. Sci. Eng. **1055**, 012090 (2021).
2) Z. Zhou, X. Chen, E. Li, L. Zeng, K. Luo, and J. Zhang, Proc. IEEE **107**, 1738 (2019).
3) W. Shi, J. Cao, Q. Zhang, Y. Li, and L. Xu, IEEE Internet Things J. **3**, 637 (2016).
4) T. Eshita, W. Wang, K. Nomura, K. Nakamura, H. Saito, H. Yamaguchi, S. Mihara, Y. Hikosaka, Y. Kataoka, and M. Kojima, Jpn. J. Appl. Phys. **57**, 11UA01 (2018).
5) J. M. Hung, C. J. Jhang, P. C. Wu, Y. C. Chiu, and M. F. Chang, IEEE J. Solid-State Circuits **1**, 171 (2021).
6) I. Khan, A. Keshavarzi, and S. Datta, Nat. Electron. **3**, 588 (2020).
7) K. Toprasertpong, E. Nako, Z. Wang, R. Nakane, M. Takenaka, and S. Takagi, Commun. Eng. **1**, 21 (2022).
8) E. Titkov, I. P. Pronin, D. V. Mashovets, L. A. Delimova, I. A. Liniichuk, and I. V. Grekhov, Semiconductors **39**, 856 (2005).
9) S. Sakai, R. Ilangovan, and M. Takahashi, Jpn. J. Appl. Phys. **43**, 7876 (2004).
10) D. Ito, N. Fujimura, T. Yoshimura, and T. Ito, J. Appl. Phys. **93**, 5563 (2003).
11) Y. Shichi, S. Tanimoto, T. Goto, K. Kuroiwa, and Y. Tarui, Jpn. J. Appl. Phys. **33**, 5172 (1994).
12) P. Wurfel and I. P. Batra, Phys. Rev. B **8**, 5126 (1973).
13) T. P. Ma and J.-P. Han, IEEE Electron Device Lett. **23**, 386 (2002).
14) D. J. Kim, J. Y. Jo, Y. S. Kim, Y. J. Chang, J. S. Lee, J. G. Yoon, T. K. Song, and T. W. Noh, Phys. Rev. Lett. **95**, 237602 (2005).
15) T. S. Böscke, J. Müller, D. Bräuhaus, U. Schröder, and U. Böttger, Appl. Phys. Lett. **99**, 102903 (2011).
16) J. Müller, T. S. Böscke, U. Schröder, S. Mueller, D. Bräuhaus, U. Böttger, L. Frey, and T. Mikolajick, Nano Lett. **12**, 4318 (2012).
17) N. Gong and T. P. Ma, IEEE Electron Device Lett. **37**, 1123 (2016).
18) E. Yurchuk, S. Mueller, D. Martin, S. Slesazeck, U. Schroeder, and T. Mikolajick, IEEE Int. Reliability Physics Symp., 2014, p. 2E.5.1, 10.1109/IRPS.2014.6860603.
19) K. Takada, S. Takarae, K. Shimamoto, N. Fujimura, and T. Yoshimura, Adv. Electron. Mater. **7**, 2100151 (2021).
20) S. Takagi, K. Toprasertpong, K. Tahara, E. Nako, R. Nakane, Z. Wang, X. Luo, T. Lee, and M. Takenaka, ECS Trans. **104**, 17 (2021).
21) Y. Hara, Mohit, T. Murakami, S. Migita, H. Ota, Y. Morita, and E. Tokumitsu, Jpn. J. Appl. Phys. **60**, SFFB05 (2021).
22) K. Hirai, T. Shiraishi, W. Yamaoka, R. Tsurumaru, Y. Inoue, and H. Funakubo, Jpn. J. Appl. Phys. **61**, SN1019 (2022).
23) Q. Tan, J. Wang, X. Zhong, Y. Zhou, Q. Wang, Y. Zhang, X. Zhang, and S. Huang, IEEE Trans. Electron Devices **58**, 2738 (2011).
24) M. Higashiwaki, K. Sasaki, H. Murakami, Y. Kumagai, A. Koukitu, A. Kuramata, T. Masui, and S. Yamakoshi, Semicond. Sci. Technol. **31**, 034001 (2016).
25) J. Green et al., APL Mater. **10**, 029201 (2022).
26) J. Zhang et al., Nat. Commun. **13**, 3900 (2022).
27) J. Noh et al., IEEE Trans. Electron Devices **68**, 2515 (2021).
28) W. Xiao, Y. Peng, S. Zheng, Q. Feng, H. Zhou, C. Zhang, J. Zhang, Y. Hao, M. Liao, and Y. Zhou, IEEE Electron Device Lett. **39**, 1504 (2018).
29) Z. Feng et al., IEEE Electron Device Lett. **41**, 333 (2020).
30) H. N. Masten, J. D. Phillips, and R. L. Peterson, J. Appl. Phys. **131**, 035106 (2022).
31) H. Zhang, R. Jia, Y. Lei, X. Tang, Y. Zhang, and Y. Zhang, J. Phys. D: Appl. Phys. **51**, 075104 (2018).
32) J. Y. Yang, J. Ma, and G. Yoo, Results Phys. **17**, 103119 (2020).
33) J. Ma and G. Yoo, IEEE Electron Device Lett. **40**, 1317 (2019).
34) L. Dong, R. Jia, C. Li, B. Xin, and Y. Zhang, J. Alloys Compd. **712**, 379 (2017).
35) J. L. Lyons, Semicond. Sci. Technol. **33**, 05LT02 (2018).
36) J. C. Hackley and T. Gougousi, Thin Solid Films **517**, 6576 (2009).
37) D. H. Triyoso, R. I. Hegde, B. E. White, and P. J. Tobin, J. Appl. Phys. **97**, 124107 (2005).
38) S. Tomer, Vandana, J. Panigrahi, R. Srivastava, and C. M. S. Rauthan, Thin Solid Films **692**, 137629 (2019).
39) S. Martin, N. Baboux, D. Albertini, and B. Gautier, Rev. Sci. Instrum. **88**, 023901 (2017).
40) S. Matsuo, T. Yamada, T. Kamo, H. Funakubo, M. Yoshino, and T. Nagasaki, J. Ceram. Soc. Jpn. **125**, 441 (2017).
41) H. Naganuma, Y. Inoue, and S. Okamura, Appl. Phys. Express **1**, 061601 (2008).
42) Y. Li, S. Deng, J. Li, G. Li, S. Zhang, and Y. Jin, Vacuum **203**, 111243 (2022).
43) Y. Xu, M. Yamazaki, and P. Villars, Jpn. J. Appl. Phys. **50**, 11RH02 (2011).
44) M. H. Lee et al., IEEE Int. Electron Devices Meeting (IEDM), p. 23.3.1, 2017, 10.1109/IEDM.2017.8268445.
45) J. Müller et al., J. Appl. Phys. **110**, 114113 (2011).
46) S. K. Lee, Y. T. Kim, S.-I. I. Kim, and C. E. Lee, J. Appl. Phys. **91**, 9303 (2002).